https://doi.org/10.5194/egusphere-2026-994
Preprint. Discussion started: 16 March 2026

Improving geolocation and footprint characterisation of microwave radiometer observations using coastal crossings

Frank Fell[1], Ralf Bennartz[2], Bruno Picard[3]

[1]Informus GmbH, 13187 Berlin, Germany
[2]Earth and Environmental Sciences, Vanderbilt University, Nashville, TN 37235-1805, United States
[3]Fluctus SAS, 81800 Rabastens, France

Correspondence to: Frank Fell (fell@informus.de)

Abstract. Spaceborne microwave radiometers (MWR) provide essential information on atmospheric humidity to enable wet tropospheric correction (WTC) in satellite altimetry. While WTC accuracy is generally high over the open ice-free ocean, it degrades in coastal areas due to land contamination in the radiometer's field of view. Correcting for this requires precise knowledge of the instrument's geolocation and spatial response characteristics.

This study presents a data-driven in-orbit approach to improve MWR geolocation and footprint characterisation for the Fundamental Data Record for Radiometry (FDR4RAD_V1), which constitutes the European Space Agency's (ESA) reference dataset of MWR observations from the ERS-1, ERS-2 and Envisat missions. By correlating observed brightness temperatures with effective land fractions at coastal transitions, we determine deviations between nominal and actual geolocation values, expressed as errors in along-track (ELON) and across-track (ECRO) direction, as well as footprint size, expressed as full width at half power (FWHP). A two-round iterative approach based on random-effects meta-analysis mitigates the effects of parameter interdependence and yields well-defined estimates with quantified uncertainties.

The analysis comprises more than 26,000 half-orbits sampled from ten repeat cycles per mission, spanning their combined full operational lifetimes (1991–2012). Substantial deviations between nominal and actual geolocations are observed for all instruments, with combined geolocation errors (ELON and ECRO via RSS) decreasing from 2.40 ± 0.07 km (ERS-1, 23.8 GHz) to 1.04 ± 0.08 km (Envisat, 23.8 GHz), indicating progressive improvements in positioning accuracy across missions. The standard errors of approximately 0.1 km, equivalent to an instrument pointing uncertainty of ~0.01°, reflect the precision achievable with this large-sample approach. For footprint size, the retrieved FWHP values range between 18.59 ± 0.04 km (Envisat, 36.5 GHz) and 21.78 ± 0.04 km (ERS-2, 36.5 GHz). Analysis of footprint geometry yields aspect ratios between 0.94 and 1.06, indicating small deviations from circularity. Temporal stability is confirmed for all mission–channel–parameter combinations except ELON for ERS-2 at 36.5 GHz, where a statistically significant trend coincides with documented gyroscope failures, revealing the method's sensitivity to platform changes.

The improved geolocation and footprint characterisation, provided for each instrument and channel, enables more accurate land contamination correction, enhancing wet tropospheric correction and sea level determination in coastal areas. The methodology is transferable to other near-nadir microwave radiometers, including those onboard the Sentinel-3 and Sentinel-6 missions, thereby supporting cross-mission consistency for multi-decadal sea-level records.

1 Introduction

1.1 The land contamination challenge in coastal altimetry

Accurate sea level monitoring is essential for assessing climate change impacts and guiding adaptation strategies for coastal regions. In this context, the combination of spaceborne radar altimetry and microwave radiometry has become a key component of ocean observation from space (Srinivasan and Tsontos, 2023). Radar altimeter observations determine the distance (range) between the satellite and the sea surface by timing the two-way travel of radar pulses and converting the resulting range measurement into sea surface height (SSH). Aggregating SSH observations over space and time yields estimates of mean sea

https://doi.org/10.5194/egusphere-2026-994
Preprint. Discussion started: 16 March 2026

level (MSL). Both global and regional MSL are recognised as Essential Climate Variables (ECVs) due to their sensitivity to ocean thermal expansion and land ice melt.

To meet stringent uncertainty requirements for SSH measurements—such as the 3.5 cm target for the Sentinel-3 mission (Drinkwater and Rebhan, 2007)—the altimeter range must be corrected for tropospheric and ionospheric path delays (Chelton et al., 2001). The most challenging of these corrections accounts for the highly variable atmospheric humidity, which induces a wet tropospheric delay (WTD) that can lead to SSH underestimation by up to 50 cm. The wet tropospheric correction (WTC) compensating for this effect is typically derived from companion passive microwave radiometers (MWRs) measuring brightness temperature (TB) at frequencies sensitive to atmospheric water vapour and cloud liquid water. Over the history of radar altimetry, two primary radiometer designs have been deployed: two-channel instruments using frequencies around 23 GHz (sensitive to water vapour) and 36 GHz (sensitive to cloud liquid water), and three-channel designs that add observations at around 18 GHz to better account for sea surface emissivity effects. Both designs exhibit footprint diameters of approximately 20–25 km and have been operated continuously since the early 1990s onwards (Srinivasan and Tsontos, 2023).

Over the ice-free open ocean, microwave radiometers enable WTC determination with an uncertainty of ~1.2 cm (Stum et al., 2011). However, in coastal areas, land coverage within the footprint significantly degrades retrieval accuracy. Because land surfaces exhibit higher microwave emissivity than water, even minor land fractions can lead to systematic WTC overestimation, particularly when located near the footprint centre where sensitivity is maximal.

Accurate coastal MSL estimates are critical as these regions often support dense populations and infrastructure highly vulnerable to sea-level rise, while exhibiting complex regional sea-level trends. Consequently, various attempts have been made to correct microwave observations in coastal areas for land contamination (e.g., Bennartz, 1999; Desportes et al., 2007; Desportes et al., 2010; Brown, 2010; Aguiar et al., 2023). While these methods differ in how they estimate land surface brightness temperature, they all require precise knowledge of the effective land fraction within the radiometer's individual footprints, which is highly sensitive to the assumed geolocation and spatial response of the sensor. An exception is the GPD+ algorithm (Fernandes et al., 2015), which circumvents this by using GNSS and numerical weather models to provide input to a data-fusion and gap-filling process.

Despite the importance of the effective land fraction as an input for contamination correction, its accurate determination is often hampered by limited pre-launch characterisation and potential in-orbit changes to the observation geometry. In this work, we present a generic, data-driven method for the in-orbit optimisation of MWR geolocation and footprint size. By correlating observed brightness temperatures with effective land coverage across coastal transitions, we retrieve geolocation errors in along-track (ELON) and across-track (ECRO) directions, as well as footprint size expressed as full width at half power (FWHP). This study provides a consistent framework for post-launch characterisation across the ERS-1, ERS-2, and Envisat missions, supporting the data continuity required for coastal sea-level climate records.

1.2 Why precise geolocation matters – a real-world example

We use a sample sea-to-land transition to illustrate how errors in the nominal geolocation of brightness temperature observations propagate into errors in the retrieved total column water vapour (TCWV) and wet tropospheric correction (WTC) in coastal areas. The underlying data are taken from the Fundamental Data Record for Radiometry (FDR4RAD_V1), further described in Sect. 2.2.

Figure 1a shows the observed brightness temperature at 23.8 GHz (TB_238) along a 1,500 km segment of ERS-1 Cycle 090, Pass 0532 (16 December 1992), extending from the North Sea (km 0) to central Spain (km 1,500), featuring five distinct coastal crossings near Middlesbrough, UK (km 110); Exeter, UK (km 570); Morlaix, France (km 800); Quimper, France (km 910); and Gijón, Spain (km 1,390).

https://doi.org/10.5194/egusphere-2026-994
Preprint. Discussion started: 16 March 2026

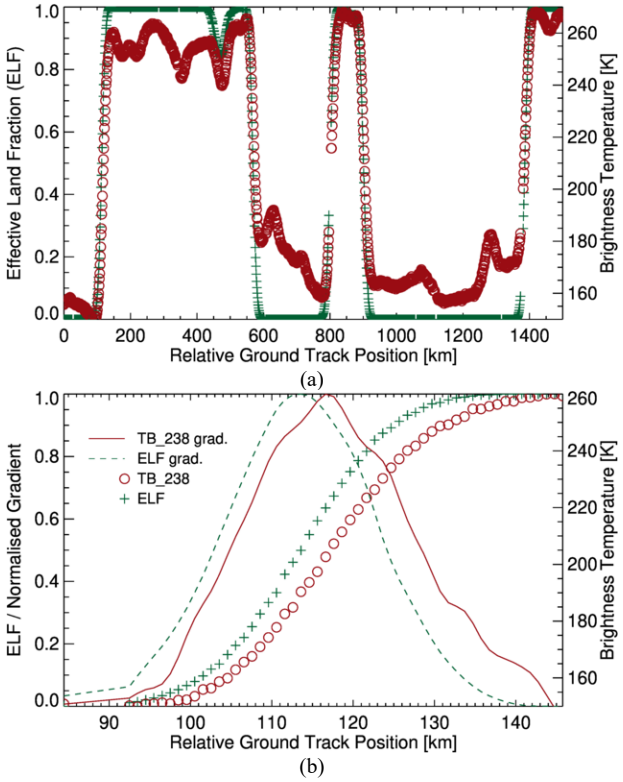

Figure 1. Comparison of 23.8 GHz brightness temperature (TB_238) and corresponding effective land fraction (ELF) for ERS-1 (Cycle 90, Pass 532 on 16 December 1992). (a) 1,500 km orbital segment from the North Sea to northern Spain showing multiple coastal transitions. (b) Detailed view of the "Yorkshire Crossing" near Middlesbrough (UK). The ELF gradient peaks ~4 km earlier than the TB_238 gradient, consistent with an along-track error (ELON) of the nominal geolocation in flight direction.

The pronounced brightness temperature contrast between land (240–270 K) and ocean (150–180 K), reflecting a typical land-water difference of ~100 K, drives a high correlation with the effective land fraction (ELF), which is derived by convolving a land-water mask with a 2D Gaussian antenna pattern as detailed in Sect. 3.1. The observed brightness temperature variations over uniform land or ocean surfaces primarily reflect changes in surface temperature and atmospheric water vapour content.

Zooming in on the first coastal crossing near Middlesbrough (the "Yorkshire Crossing"), Fig. 1b highlights the strong correlation between TB_238 and ELF, both exhibiting a sigmoid-like increase from water to land. However, there is a noticeable spatial offset: ELF rises earlier than TB_238, consistent with the existence of an along-track error (ELON) in the nominal geolocation of the observations' effective footprint centre. Based on the distance between the TB_238 and ELF gradient peaks, ELON is estimated to be on the order of +4 km for this particular case, where the positive sign indicates a shift in flight direction. *Note that ELON values determined from individual coastal crossings include apparent contributions from across-track errors (ECRO), as further discussed in Sect. 3.3.1.*

Errors in footprint geolocation critically compromise land contamination correction procedures that rely on accurate footprint positioning. For the presented example, ELF increases by ~0.9 over ~30 km, implying an average coastal ELF gradient of ~0.03 km^{-1}. An along-track geolocation error δ_ELON of 1 km thus induces an error of δ_ELF ≈ 0.03, translating into a brightness temperature error of δ_TB ≈ 3 K, given a land-sea brightness temperature difference ($\Delta TB_{L\text{-}W}$) of 100 K. Propagating this δ_TB through the 23.8 GHz water vapour sensitivity ($\partial TB/\partial TCWV \approx 0.8 – 1.7$ K $(kg\ m^{-2})^{-1}$; Obligis et al., 2006) yields a moisture error of δ_TCWV ≈ 1.8 kg – 3.8 kg m^{-2} for dry and wet atmospheric conditions, respectively. Finally,

https://doi.org/10.5194/egusphere-2026-994
Preprint. Discussion started: 16 March 2026

applying the relation ΔWTC (cm) ≈ −0.64 × ΔTCWV (kg m^{-2}) provided by Bevis et al. (1992) gives the corresponding error δ_WTC ≈ −1.1 cm to −2.4 cm.

Geolocation errors as small as 1 km thus induce centimetre-level WTC uncertainties in coastal zones, contributing significantly to total WTC uncertainty. To enable accurate land contamination correction, it is essential to reconcile nominal geolocations with the true effective footprint centres.

2 Instruments and data

2.1 The Microwave Radiometer onboard ERS-1, ERS-2, and Envisat

The European Space Agency's (ESA) ERS-1, ERS-2, and Envisat missions established a continuous archive of Earth observation data between 1991 and 2012, providing the observational baseline necessary for characterizing global sea level trends, polar ice dynamics, and ocean-atmosphere interactions. To achieve the envisaged high precision in altimetry, each platform carried a near-nadir pointing Dicke-type Microwave Radiometer (MWR) operating in two channels at 23.8 GHz and 36.5 GHz with footprint diameters on the order of 20 km, varying slightly by instrument and channel. While ERS-1 and ERS-2 shared identical designs (Eymard et al., 2005), Envisat's MWR featured structural and electronic upgrades for enhanced calibration performance (Atkinson et al., 1998).

2.1.1 MWR footprint characterisation

Technical documentation on MWR instrument characteristics for heritage missions is limited in the open literature. Notably, the most comprehensive documentation exists for the earliest mission, with Bernard et al. (1993) providing detailed pre-launch characterisation of ERS-1's MWR antenna patterns, which also apply to ERS-2 due to identical hardware design (Eymard et al., 2005). For Envisat's MWR, relevant information is found in the Envisat RA2/MWR Product Handbook (ESA, 2007). In accordance with the original documentation, we cite the 3-dB beamwidth in Table 1, while the equivalent term FWHP is adopted throughout the remainder of this study.

Table 1. Footprint characterisation of the MWR instruments onboard ERS-1, ERS-2, and Envisat. Operational period information is taken from FDR4ALT-MWR (2024). FWHP is expressed as along-track × across-track dimensions. For Envisat, the 3-dB beamwidth is specified at 1.5°, which is converted to linear distances (km) assuming a nominal flight altitude of 800 km.

Mission	MWR operational period	Channel (GHz)	3-dB beamwidth (km)	Off-nadir pointing (degree)	Reference
ERS-1	1991/07 -1996/06	23.8	21.2 × 21.2	1.93, backward	Bernard et al., 1993
ERS-1	1991/07 -1996/06	36.5	22.5 × 19.1	2.50, forward	Bernard et al., 1993
ERS-2	1995/04 - 2011/07	23.8	21.2 × 21.2	1.93, backward	Eymard et al., 2005
ERS-2	1995/04 - 2011/07	36.5	22.5 × 19.1	2.50, forward	Eymard et al., 2005
Envisat	2002/03 - 2012/04	23.8	~(20.9 × 20.9)	1.83, backward	ESA, 2007
Envisat	2002/03 - 2012/04	36.5	~(20.9 × 20.9)	1.72, forward	ESA, 2007

https://doi.org/10.5194/egusphere-2026-994
Preprint. Discussion started: 16 March 2026

2.1.2 Pointing errors

MWR geolocation uncertainty is dominated by attitude-related errors. For ERS-1, systematic attitude errors of ≤0.11° (pitch/roll) and ≤0.21° (yaw), plus harmonic and random errors of ≤0.03° (pitch/roll) and ≤0.07° (yaw) are reported (https://www.eoportal.org/satellite-missions/ers-1#spacecraft, last access: 5 January 2026). Combining these via root-sum-square (RSS) yields maximum angular offsets of ~0.13° (pitch/roll) and ~0.22° (yaw), equivalent to ~3.5 km total pointing uncertainty at the surface given the ~800 km orbital altitude. Orbit determination errors (radial: 5 m, cross-track: 15 m, along-track: 60 m) reported by the same source and potential timing-related biases (e.g., 7 m for an assumed 1 ms delay at 7 km s^{-1} ground speed) contribute <5 % to the total geolocation uncertainty. ERS-2, sharing the ERS-1 platform design, is assumed to exhibit similar performance. While Envisat's advanced attitude control systems are expected to result in reduced pointing errors, specific quantitative values for Envisat's pointing errors could not be found in the open literature. Consequently, we attribute the observed systematic discrepancies between the effective footprint centres and the nominal geolocation primarily to these pointing errors.

2.2 The FDR4ALT Fundamental Data Record for Radiometry

The FDR4ALT (Fundamental Data Records for Altimetry) datasets, generated within ESA's Long Term Data Preservation (LTDP+) programme, constitute the current reference for the ERS-1/2 and Envisat missions, superseding all previous data releases (https://earth.esa.int/eogateway/catalog/fdr-for-radiometry, last access 26 January 2026). The FDR4ALT product family comprises two Fundamental Data Records (FDR) for both radar altimetry and microwave radiometry, as well as six Thematic Data Products (TDP) covering various geophysical domains, including ocean, land ice, and atmosphere.

We utilise Version 1 of the Fundamental Data Record for Radiometry (FDR4RAD_V1), which provides intercalibrated top-of-atmosphere brightness temperatures at 23.8 GHz (TB_238) and 36.5 GHz (TB_365) at the MWR's 7 Hz native acquisition rate, yielding sequential observations spaced approximately 1 km along-track. Compared to the earlier REAPER (Reprocessing of Altimeter Products for ERS) dataset (Brockley et al., 2017), FDR4RAD_V1 features algorithmic refinements, improved antenna sidelobe corrections, advanced flagging, and gap-filling techniques to enhance data quality and coverage (Piras et al., 2023). Released publicly in 2023 (FDR4ALT-MWR, 2024), the dataset organises observations into pole-to-pole half-orbit (ascending or descending passes) NetCDF files. For analysis, we extract the variables *longitude*, *latitude*, *distance_to_coast*, *tb_238* and *tb_365* from the *main* data group.

For each channel and mission, we selected ten full repeat cycles distributed across the respective mission's lifetime to enable the detection of potential instrumental drifts. Most cycles span 35 days and nominally comprise 1,002 passes (35 days × 14.3 orbits per day × 2 passes per orbit), with the exception of four ERS-1 3-day cycles (two in 1991 and two in 1994) comprising between 81 and 108 passes. Table A1 in Appendix A provides the complete list of repeat cycles analysed.

2.3 Ancillary data and tools

Information on the global land-sea distribution is obtained from the Global Land Mask for Satellite Ocean Colour Remote Sensing (Mikelsons et al., 2021), offering 480 data points per degree (~230 m equatorial resolution), adequate for resolving complex coastlines when convolving them with MWR-sized antenna footprints. To enhance processing efficiency, the mask was converted from its native NetCDF format to tiled GeoTIFF using the *gdal_translate* utility from the Geospatial Data Abstraction Library (GDAL) version 3.8.3 (Rouault et al., 2025).

Coastal orientation is critical for analysing land-sea transitions, as it determines the satellite track's incidence angle relative to the coast, which governs both the geometric length of coastal transitions and the resulting gradients in brightness temperature and effective land fraction. We utilise coastal orientation data from the Global Coastal Characteristics (GCC) dataset, which characterises 728,088 km of global coastline at 1 km resolution (Athanasiou et al., 2024).

https://doi.org/10.5194/egusphere-2026-994
Preprint. Discussion started: 16 March 2026

3 Retrieval parameters

3.1 Modelling the effective land fraction

Any observation by a spaceborne microwave radiometer represents a convolution of the top-of-atmosphere brightness temperature field with the instrument's true antenna pattern. The corresponding effective land fraction (ELF) is obtained from an equivalent convolution of the modelled antenna pattern with a binary land-sea mask (see Appendix B for the mathematical formulation). By comparing these modelled ELF values to the observed brightness temperatures (TB), we can characterise systematic geolocation discrepancies.

Because the MWRs are near-nadir-pointing instruments and since this study utilises brightness temperature observations corrected for sidelobe effects (Sect. 2.2), the antenna pattern used for calculating ELF is approximated as 2D Gaussian representing the main lobe, truncated at a diameter of $c \times$ FWHP.

Antenna pattern sensitivity is specified as a function of distance to the beam centre in Cartesian space, while global land-sea masks use geographic coordinates (latitude-longitude). Consequently, we perform a coordinate transformation at each footprint location prior to convolution. For our statistical approach which requires processing a large ensemble of global coastal crossings, a spatial resolution of 1 km and a truncation factor of $c = 2.5$ (yielding 98.7 % enclosed power) provide sufficient accuracy at manageable computational cost.

3.2 Retrieval approach and target parameters

The main aspects governing geolocation optimisation of MWR observations are introduced in Sects. 3.2 to 3.4. Figures 2 to 5 illustrate these concepts using consistent graphical conventions listed in Panel 1.

Panel 1: Graphical conventions for MWR geolocation analysis. Symbols and logic used consistently across Figs. 2 to 5. The scheme distinguishes between the physical MWR observation (red) and the synthetic parameters used for effective land fraction (ELF) modelling (green).

Category	Symbol	Explanation
Motion	Black line with arrow (dashed / dotted)	Satellite ground track (nominal / alternative)
Surface	Light grey horizontal hatching	Water
	Dark grey diagonal hatching	Land
	Dark grey solid line	Coastline
MWR observation	Red dot	Observed effective centre
	Radial gradient, red to orange	Actual MWR sensitivity (2.5×FWHP)
ELF modelling	Green dot	Modelled footprint centre
	Green circle	Synthetic footprint area for ELF calculation
	Line style solid / dashed	At nominal / shifted geolocation
	Line weight thick / thin	Matching / non-matching with MWR
Errors	Red arrow (solid / dashed)	True error (ELON / ECRO)
	Blue arrow (solid / dashed)	Apparent error ($ELON_{APP}$ / $ECRO_{APP}$)
	Purple arrow (solid / dashed)	Observed error ($ELON_{OBS}$ / $ECRO_{OBS}$)

In an ideal scenario (Fig. 2a), the effective centre and the actual extent of the radiometer footprint align with its nominal geolocation and assumed extent used for ELF modelling, maximising the correlation between the observed brightness temperature (TB) and the modelled ELF along the coastal crossing.

https://doi.org/10.5194/egusphere-2026-994
Preprint. Discussion started: 16 March 2026

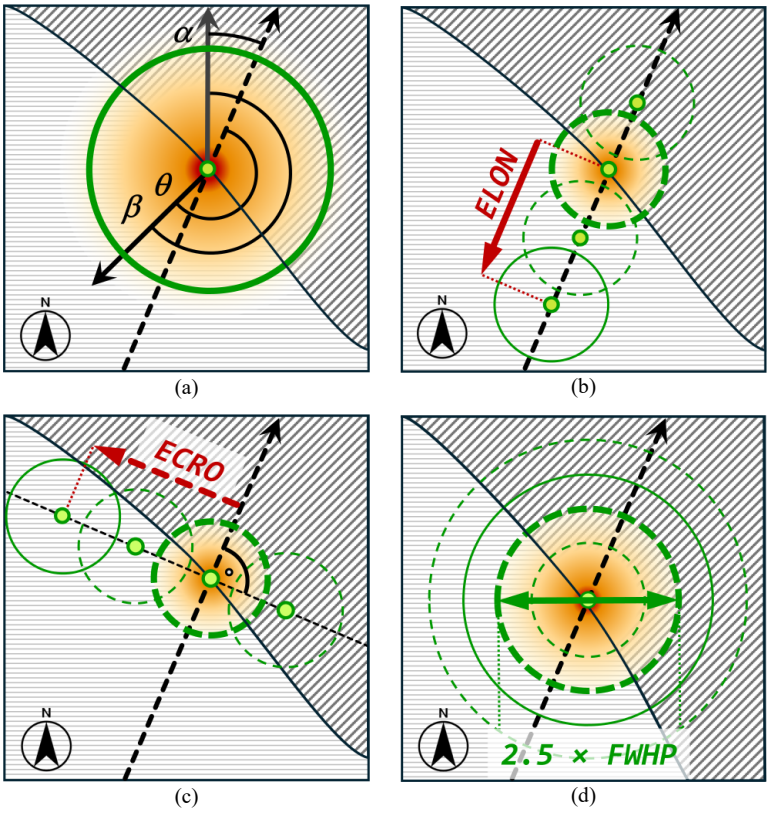

Figure 2. Retrieval scenarios for ELON, ECRO, and FWHP. (a) Ideal scenario under coastal crossing angle $\theta = \beta - \alpha$, where α is the local orbital azimuth and β the coastal orientation. (b) Along-track error where the nominal footprint position lags behind the true position by distance ELON. (c) Across-track error with the nominal footprint position shifted in flight direction leftward by distance ECRO. (d) Footprint size estimation procedure. See Panel 1 for graphical conventions.

In practice, deviations between true and nominal geolocation, as well as between the actual footprint size and the footprint model used for ELF calculation, reduce this correlation. The analysis of coastal crossings enables the quantification of these deviations through three optimisation parameters:

- ELON, the along-track geolocation error (Fig. 2b);
- ECRO, the across-track geolocation error (Fig. 2c);
- FWHP, the width of the footprint model tuned to best represent the true footprint size (Fig. 2d).

The following subsections describe how these parameters are determined from individual coastal crossings.

3.2.1 Along-track error (ELON)

Figure 2b illustrates a scenario where the nominal geolocation lags behind the actual footprint's centre, reducing TB–ELF correlation along the coastal crossing: The actual radiometer footprint is centred over the coastline (ELF ≈ 0.5), while the modelled footprint at the nominal geolocation remains entirely over water (ELF = 0.0).

To quantify ELON, we shift the modelled footprint along the ground track until TB–ELF correlation peaks. The resulting displacement between the nominal geolocation and this optimal position defines the along-track error. By convention, positive ELON indicates the nominal geolocation leads the true footprint position, while negative values denote a lag.

https://doi.org/10.5194/egusphere-2026-994
Preprint. Discussion started: 16 March 2026

3.2.2 Across-track error (ECRO)

Figure 2c shows a scenario where the nominal geolocation is offset to the left from the actual footprint (relative to the flight direction), reducing TB–ELF correlation along the coastal crossing: The actual radiometer footprint is centred over the coastline (ELF ≈ 0.5), while the modelled footprint centred at the nominal geolocation remains mostly over water (ELF < 0.05).

To quantify ECRO, we shift the modelled footprint perpendicular to the ground track until TB–ELF correlation peaks. The resulting displacement between the nominal geolocation and this optimal position defines the across-track error. By convention, positive ECRO indicates a leftward offset of the nominal geolocation relative to flight direction, while negative values denote an offset to the right.

3.2.3 Footprint size (FWHP)

Figure 2d presents a scenario with perfect geolocation alignment but varying size of the modelled footprint. Underestimated sizes produce unrealistically sharp ELF coastal transitions, whereas overestimated sizes cause excessive smoothing – both inconsistent with brightness temperature measurements integrating the actual antenna sensitivity.

To optimise the footprint model, we vary FWHP around the nominal value until TB–ELF correlation is maximised. This optimal FWHP value identifies the footprint model that most closely approximates the physical observation geometry, given the assumptions of a 2D Gaussian sensitivity extending to 2.5 × FWHP.

3.3 Retrieval challenges

The retrieval of ELON, ECRO, and FWHP is inherently ill-posed for individual observations, primarily due to two fundamental challenges:

(1) Parameter interdependence (crosstalk): For individual coastal crossings, the retrieval accuracy of any single parameter (ELON, ECRO, FWHP) is intrinsically linked to the uncertainties of the other two.

(2) Solution ambiguity (degeneracy): Multiple, distinct combinations of ELON and ECRO can produce near-identical observational signatures, preventing the unambiguous determination of these parameters from single overpasses.

The following subsections analyse these challenges and present mitigation strategies to overcome them.

3.3.1 Parameter interdependence

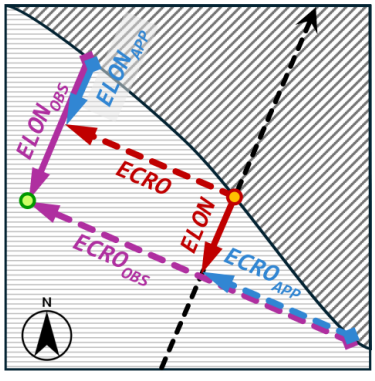

Figure 3. Interdependence of ELON and ECRO. The combination of true and apparent errors produces the values retrieved from individual crossings. See Panel 1 for graphical conventions.

https://doi.org/10.5194/egusphere-2026-994
Preprint. Discussion started: 16 March 2026

Figure 3 demonstrates the interdependence of ELON and ECRO for individual coastal crossings:

- A true along-track error (ELON) generates an apparent across-track error ($ECRO_{APP}$).
- A true across-track error (ECRO) generates an apparent along-track error ($ELON_{APP}$).

Consequently, the observed values comprise both true and apparent components:

$$ELON_{OBS} = ELON + ELON_{APP}, \quad (1)$$

$$ECRO_{OBS} = ECRO + ECRO_{APP} \quad (2)$$

Coastal geometry controls both direction and magnitude of the apparent errors (Sect. 3.4). Importantly, these tend to cancel out when averaged across a wide range of coastal crossing angles (Sect. 5.2), while true errors converge to stable values. A weaker interdependence links position and footprint size: inaccuracies in one degrade the retrieval precision of the other, though iterative refinement improves both (Sect. 5.3.1).

3.3.2 Retrieval ambiguities

Simultaneous retrieval of ELON and ECRO from individual coastal crossings is fundamentally limited by mathematical degeneracy—distinct parameter combinations that yield nearly identical TB—ELF correlation maxima. FWHP degeneracy is weaker, as variations in footprint size primarily alter the shape of ELF extrema rather than their position along the satellite track, with correspondingly smaller impact on TB—ELF correlation.

For example, when crossing a linear coastline under idealised conditions (horizontal homogeneity), any shift in geolocation that positions the footprint centre onto the coastline produces indistinguishable TB—ELF correlation maxima, preventing simultaneous parameter determination of ELON and ECRO (Fig. 4a).

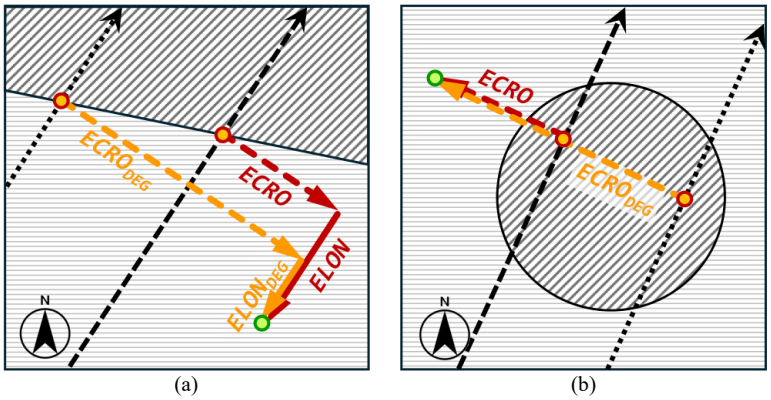

(a) (b)

Figure 4. Degenerate solutions under idealised conditions. (a) Linear coastline: Both the true solution (ELON, ECRO) and a degenerate counterpart ($ELON_{DEG}$, $ECRO_{DEG}$) both position the footprint centre on the coastline, yielding identical TB—ELF correlation signatures. (b) Circular island: Symmetric overpasses integrate identical proportions of land and water, making the true across-track error (ECRO) indistinguishable from its symmetric counterpart ($ECRO_{DEG}$). See Panel 1 for graphical conventions.

Individual parameters can also exhibit intrinsic ambiguities. For instance, when crossing a circular island, overpasses symmetric about the island's centre integrate identical proportions of land and water, creating degenerate ECRO solutions (Fig. 4b).

While complex coastal morphologies (e.g., archipelagos) provide more unique features that break these symmetries, they introduce additional challenges, as overlapping signals may produce multiple local TB—ELF correlation maxima that mask

https://doi.org/10.5194/egusphere-2026-994
Preprint. Discussion started: 16 March 2026

the true geolocation error. Consequently, retrieval ambiguity is resolved through sequential optimisation, i.e., by fixing two parameters to provide a stable baseline while solving for the third.

3.4 Impact of coastline orientation

The retrieval accuracy of ELON and ECRO critically depends on the coastal crossing angle $\theta = \beta - \alpha$, where α is the satellite's ground track azimuth and β denotes the local coastline orientation (seaward-pointing normal vector), both measured clockwise from true North (Fig. 2a). For linear coastlines under locally homogeneous conditions, the interdependence between true and apparent geolocation errors is expressed by:

$$\mathrm{ELON}_{\mathrm{APP}} = \tan(\theta) \times \mathrm{ECRO}\,, \tag{3}$$

$$\mathrm{ECRO}_{\mathrm{APP}} = \cot(\theta) \times \mathrm{ELON}\,. \tag{4}$$

Near-orthogonal coastal crossings ($\theta \approx 180°$ for sea-to-land, $\theta \approx 0°$ for land-to-sea) minimise the contribution of ECRO to $\mathrm{ELON}_{\mathrm{APP}}$ (Fig. 5a), while maximising TB and ELF gradients across the coast, enabling robust ELON retrieval.

ECRO retrieval is more challenging. While near-parallel crossings ($\theta \approx 90°$ and $\theta \approx 270°$) minimise the contribution of ELON to $\mathrm{ECRO}_{\mathrm{APP}}$ (Fig. 5b), these angles also extend the spatial distance over which the coastal transition occurs, reducing TB and ELF gradient magnitudes, thereby degrading correlation optimisation precision. The optimal crossing angle for ECRO retrieval therefore occurs at intermediate angles balancing minimal parameter coupling with adequate gradient strength (Sect. 5.4.1).

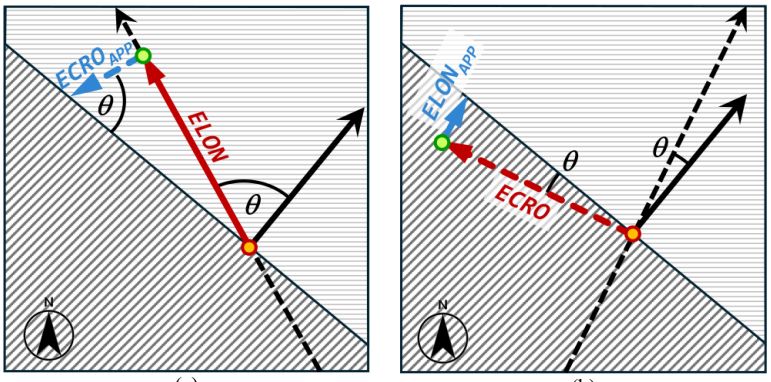

Figure 5. Dependence of apparent geolocation errors on the coastal crossing angle θ. (a) Near-orthogonal crossings minimise ECRO contributions to $\mathrm{ELON}_{\mathrm{APP}}$. (b) highly oblique angles minimise ELON contributions to $\mathrm{ECRO}_{\mathrm{APP}}$. See Panel 1 for graphical conventions.

4 Processing individual coastal crossings

4.1 Identification of suitable coastal crossings

To identify coastal crossings suitable for the determination of ELON, ECRO, and FWHP, we apply a multi-stage filtering process to the pole-to-pole half-orbit files to identify high-contrast transitions while ensuring sufficient data density for statistical significance:

(1) Sea ice exclusion: Observations poleward of 45° N/S are rejected to prevent sea ice from introducing false correlation maxima. (This criterion is waived for case studies with confirmed ice-free conditions.)

https://doi.org/10.5194/egusphere-2026-994
Preprint. Discussion started: 16 March 2026

(2) Coastal proximity: Observations further than 30 km (~1.5 × FWHP) from the nearest coastline, both landward and seaward, are excluded to reduce data volume while preserving the full ELF range from zero to one.

(3) Fragmentation: After applying filters (1) and (2), sequential observations within 5 km (~0.25 × FWHP) are grouped into single crossing events to maintain spatial continuity while minimising fragmentation.

(4) Sample size: Crossings with fewer than 20 observations within ELF ∈ [0.01, 0.99] are discarded to ensure adequate statistical power for correlation optimisation and uncertainty estimation.

(5) Spatial extent: Crossings spanning more than 120 km are rejected to limit the impact of surface or atmospheric inhomogeneities. This criterion inherently eliminates overpasses at highly oblique crossing angles.

(6) ELF range: Crossings with an ELF range below 0.5 are discarded to ensure adequate TB—ELF contrast for correlation optimisation.

Typically, each orbital pass yields 1.5–2.0 suitable crossings, providing a sufficient global sample size for the statistical analysis in Sect. 6.

4.2 Parameter retrieval

We retrieve $ELON_{OBS}$, $ECRO_{OBS}$, and $FWHP_{OBS}$ by maximising Pearson's correlation coefficient r between the observed brightness temperature and the modelled ELF. Following the logic in Sect. 3.3.2, each parameter is optimised independently while holding non-target parameters at their nominal values.

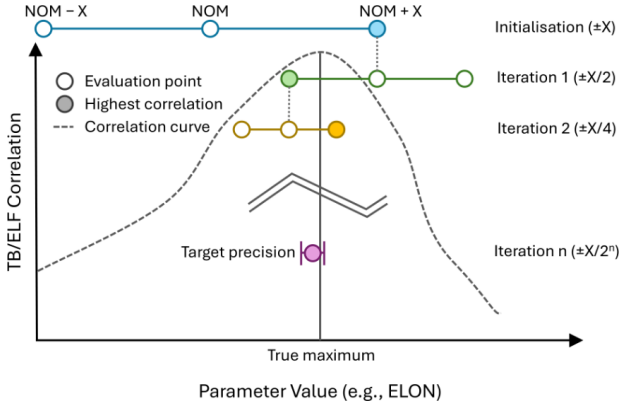

Figure 6. Iterative bracketing approach for parameter retrieval. The search centre drifts adaptively as the bracket width halves in each iteration, eventually converging on the optimal parameter value within the target precision.

We employ an iterative bracketing approach (Fig. 6) for computational efficiency. The algorithm evaluates TB—ELF correlations at three positions $[NOM - X, NOM, NOM + X]$, where NOM initially represents the nominal value (0 km for ELON and ECRO, and 20 km for FWHP), and the bracket size $\pm X$ encompasses expected parameter variation. In subsequent iterations, the search is re-centred on the position providing the highest correlation from the previous iteration while halving the bracket width. This process continues until achieving the target precision.

The specific search ranges used are:

- ELON and ECRO: $X = 12.8$ km and $NOM = 0.0$ km, providing an initial bracket of [–12.8, +12.8] km, halved eight times to achieve 50 m precision within a [−25.55, +25.55] km search range.
- FWHP: $X = 6.4$ km and $NOM = 20.0$ km, providing an initial bracket of [13.6, 26.4] km, halved seven times to achieve 50 m precision within a [7.25, 32.75] km search range.

https://doi.org/10.5194/egusphere-2026-994
Preprint. Discussion started: 16 March 2026

In either case, the search centre drifts adaptively within the respective full search ranges. Each optimisation also yields the corresponding correlation coefficient, along with ancillary metadata (e.g., crossing angle, location) for subsequent statistical analysis.

While this approach may occasionally miss absolute correlation maxima in complex coastal geometries with multiple peaks, it provides an effective balance between computational efficiency and retrieval accuracy. Crossings where the maximum correlation falls outside the full search range are considered morphologically complex and excluded from further analysis.

4.3 The Yorkshire Crossing case study

We demonstrate the retrieval logic using the "Yorkshire Crossing" introduced in Sect. 1.2. This non-idealised case illustrates the practical application of the method and the varying sensitivity of the three optimisation parameters in response to the local crossing geometry and coastal morphology. To better visualise the correlation response, we replace the iterative bracketing approach of Sect. 4.2 with equally spaced coordinate shifts.

On 16 December 1992 (Cycle 90, Pass 532), ERS-1 crossed the Yorkshire (UK) coast from NE to SW close to Middlesbrough at a near-orthogonal angle ($\theta \approx 170°$), with TB_238 rising from ~150 K over the North Sea to ~260 K inland (Fig. 7). The coastal morphology within the TB_238 footprints is complex, with the River Tees estuary as a notable feature to the right of the flight path.

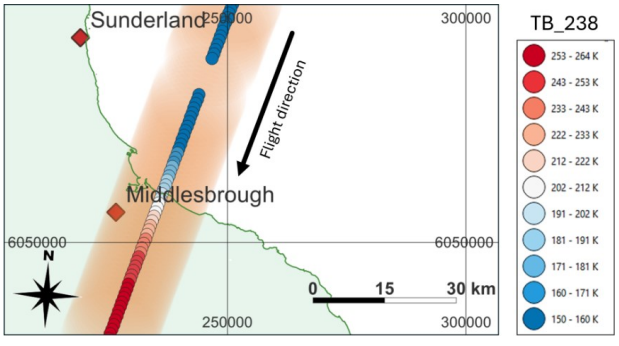

Figure 7. ERS-1 TB_238 for the Yorkshire Crossing. Individual observations are shown as coloured circles; orange shading indicates the approximate FWHP extent (20.0 km). The ~8 km data gap offshore results from regular data acquisition interruptions specific to ERS-1. Geographic coordinates in UTM 31N.

4.3.1 Assessing the along-track error

The retrieval of the along-track error ELON is demonstrated in Fig. 8, with ECRO and FWHP held at their nominal values (0 km and 20 km, respectively).

Figure 8a compares TB_238 observations (red circles) with the corresponding ELF (green crosses) at the nominal geolocation. The spatial mismatch is evident: when approaching the coast, ELF rises earlier than TB_238, suggesting the nominal geolocation leads the true footprint position. The coloured lines show ELF values when the nominal geolocation is systematically moved along-track: forward shifts (dashed purple) and backward shifts (solid green) in 2 km increments up to ±12 km.

Figure 8b quantifies this mismatch through correlation analysis. The vertical orange line marks the TB_238-ELF correlation at the nominal geolocation. As geolocation is shifted backward (negative shifts), the correlation increases, reaching a maximum ($r > 0.999$) at approximately -5 km, indicating that the nominal geolocation leads the true footprint centre by ~5 km, yielding $ELON_{OBS} \approx +5$ km for this particular crossing, in line with the + 4 km estimate obtained from visual assessment in Fig. 1b.

https://doi.org/10.5194/egusphere-2026-994
Preprint. Discussion started: 16 March 2026

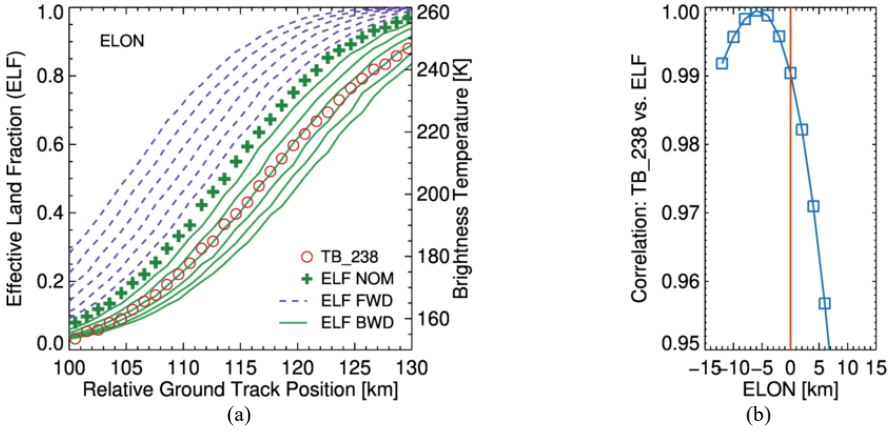

Figure 8. Retrieval of the along-track geolocation error ELON for the Yorkshire Crossing. (a) ERS-1 TB_238 observations compared to ELF at the nominal geolocation and footprint size and along-track geolocations shifted in forward (FWD) or backward (BWD) directions, extending to ±12 km in 2 km increments. (b) TB_238-ELF correlation as a function of the along-track geolocation shift. The peak identifies the observed error $ELON_{OBS}$, while the vertical orange line marks the correlation at the nominal position.

4.3.2 Assessing across-track error and footprint size

The retrieval of ECRO and FWHP follows the same sequential logic, with non-target parameters held at nominal values.

For ECRO, the correlation response is broader than for ELON, reaching a lower maximum $r \approx 0.995$ at a rightward shift of approximately +8 km, yielding $ECRO_{OBS} \approx$ -8 km. This reduced sensitivity reflects the weaker geometric constraints for across-track error determination during near-orthogonal coastal crossings, consistent with the theoretical framework in Sect. 3.4.

For FWHP, the correlation peaks at approximately 26 km, which is larger than the nominal 20 km. The correlation response is asymmetric: undersized footprints degrade the correlation more rapidly than oversized ones. The lower peak correlation ($r \approx 0.992$) compared to both ELON and ECRO suggests that FWHP retrieval is particularly sensitive to geolocation error interdependence; residual offsets in the spatial coordinates constrain the correlation maximum, as any misregistration prevents the modelled ELF gradient from fully capturing the observed brightness temperature transition.

4.3.3 Case study conclusions

The Yorkshire Crossing analysis reveals marked differences in parameter retrieval sensitivity. $ELON_{OBS}$ exhibits the highest correlation ($r > 0.999$) with a sharp, well-defined peak, making it the most reliably determined parameter. Conversely, $ECRO_{OBS}$ ($r \approx 0.995$) and $FWHP_{OBS}$ ($r \approx 0.992$) exhibit broader correlation functions with lower maxima, indicating reduced retrieval precision.

This individual case study proves the viability of the sequential optimisation approach but also demonstrates that a single overpass is insufficient for a definitive sensor characterisation. Robust determination of true ELON, ECRO and FWHP requires a statistical aggregation across an ensemble of crossings with varying geometries and environmental conditions, allowing the effects of parameter interdependence and the impact of transient environmental non-uniformity to cancel through averaging, as discussed in Sect. 5.2.

https://doi.org/10.5194/egusphere-2026-994
Preprint. Discussion started: 16 March 2026

5 Statistical aggregation

5.1 The need for statistical aggregation

The Yorkshire Crossing example highlights the challenges of retrieving ELON, ECRO, and FWHP from individual coastal crossings, particularly those arising from coastline orientation and error interdependence. Other challenges include spatial inhomogeneities in surface brightness temperature and atmospheric moisture fields, complex coastline morphologies, varying land-sea distribution in tidal flats, as well as inaccuracies in the applied land-sea mask.

To overcome these challenges, we adopt a statistical approach leveraging a large number of coastal crossings encompassing a wide range of coastal geometries and environmental conditions, offering the following key advantages:

- Error decorrelation: Interdependence between errors tends to cancel out when averaged over a nearly uniformly distributed range of crossing angles (Sect. 5.2).
- Noise reduction: Transient phenomena (e.g., local TB gradients) and residual random fluctuations inherent in individual retrievals diminish through aggregation.
- Selection bias elimination: By applying objective, automated criteria, we eliminate selection bias and capture the full spectrum of real-world coastal complexity.

The statistical retrieval approach yields a robust evaluation framework independent of individual crossing characteristics and resilient to localised anomalies. The large sample sizes provide robust uncertainty quantification and enable systematic errors to become apparent, while the temporal coverage allows detection of potential drifts in instrument characteristics.

5.2 Cancellation of apparent errors

The dependency of $ELON_{APP}$ on the tangent of the coastal crossing angle θ in Eq. (3) implies it adopts additive inverses (same magnitude, opposite sign) when θ is mirrored at 0° for land-to-sea, or 180° for sea-to-land transitions. Similarly, $ECRO_{APP}$'s dependency on cot θ in Eq. (4) causes it to adopt additive inverses when θ is mirrored at 90° for land-to-sea, or 270° for sea-to-land transitions. Therefore, if coastal crossing angles were uniformly distributed, both $ELON_{APP}$ and $ECRO_{APP}$ would cancel when aggregated over a sufficient number of samples, enabling stable retrievals of ELON and ECRO despite their interdependence in individual observations.

The frequency of coastal crossings scales approximately as $|\cos(\theta)|$, reflecting the projected coastline length perpendicular to the satellite track. For example, a coastal segment perpendicular to the satellite track ($\theta = 0°$) is on average crossed twice as often as an equal-length segment at $\theta = 60°$. Consequently, ELON aggregation benefits from abundant perpendicular crossings with favourable retrieval conditions, whereas ECRO relies on less frequent oblique crossings, limiting its retrieval accuracy.

Figure 9a illustrates this angular dependency for 453 coastal crossings from 250 randomly selected passes from ERS-1 Cycle 090 meeting the quality criteria defined in Sect 4.1. The histogram reflects the theoretical $|\cos(\theta)|$ distribution, with maxima around 0° and 180° (near-perpendicular crossings) and minima around 90° and 270° (near-parallel crossings), demonstrating the statistical challenges for ECRO retrieval.

The Global Coastal Characteristics (GCC) dataset (Athanasiou et al., 2024) — an inventory of 728,088 km of coastlines at 1 km resolution—exhibits relatively uniform global coastline orientation (Fig. 9b): an average length of 2,022 ± 146 km per degree coastal orientation, with roughly ±20 % variation across azimuthal bins (from 1,635 km per degree for azimuths 349°–350° to 2,419 km per degree for azimuth 273°–274°). This near-uniformity ensures effective cancellation of error interdependence in ensemble-based retrievals.

https://doi.org/10.5194/egusphere-2026-994
Preprint. Discussion started: 16 March 2026

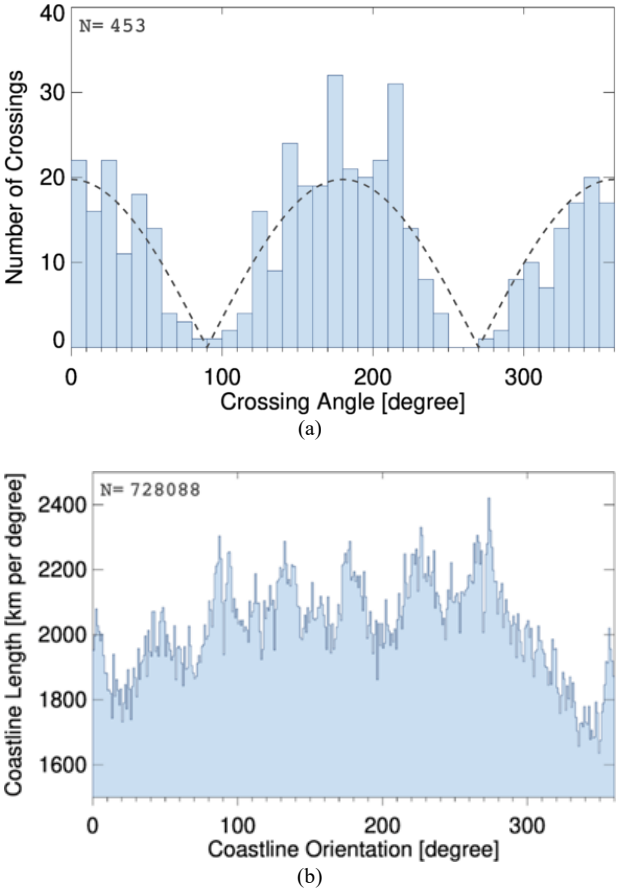

Figure 9. (a) Coastal crossing angles for 453 land/sea transitions from ERS-1 Cycle 090, together with the theoretical |cos(*θ*)| distribution. (b) Coastline length per degree coastline orientation (Athanasiou et al., 2024).

5.3 Statistical aggregation framework

We implement a hierarchical framework to derive robust estimates of ELON, ECRO, and FWHP from individual coastal crossings. The approach combines a random-effects meta-analysis to account for within- and between-cycle variability with an iterative refinement procedure to reduce parameter interdependence and the associated uncertainty.

5.3.1 Random-effects meta-analysis

We determine mission- and channel-specific parameters in two stages, using ten repeat cycles per mission (Table A1). Our approach is based on a variance model (Sect. 5.4) that assigns a precision to each individual retrieval based on its coastal crossing angle.

In the first stage, individual retrievals ($ELON_{OBS}$, $ECRO_{OBS}$, $FWHP_{OBS}$) within a single cycle are combined using the arithmetic mean. This ensures the estimate remains robust against potential weighting biases, while the individual variances are aggregated to obtain a corresponding per-cycle adjusted variance (Appendix C1). The underlying assumption is that all crossings within a cycle sample a common underlying parameter value, with differences arising solely from random measurement variation.

https://doi.org/10.5194/egusphere-2026-994
Preprint. Discussion started: 16 March 2026

In the second stage, per-cycle estimates are combined via a random-effects meta-analysis based on the DerSimonian–Laird estimator (Borenstein et al., 2021), accounting for potential between-cycle heterogeneity arising from instrumental drift, longer-term environmental variations, or other systematic differences (Appendices C2 and C3).

5.3.2 Iterative refinement

To reduce interdependence and the associated uncertainties, the random-effects meta-analysis from Sect. 5.3.1 is applied in two successive rounds (Fig. 10).

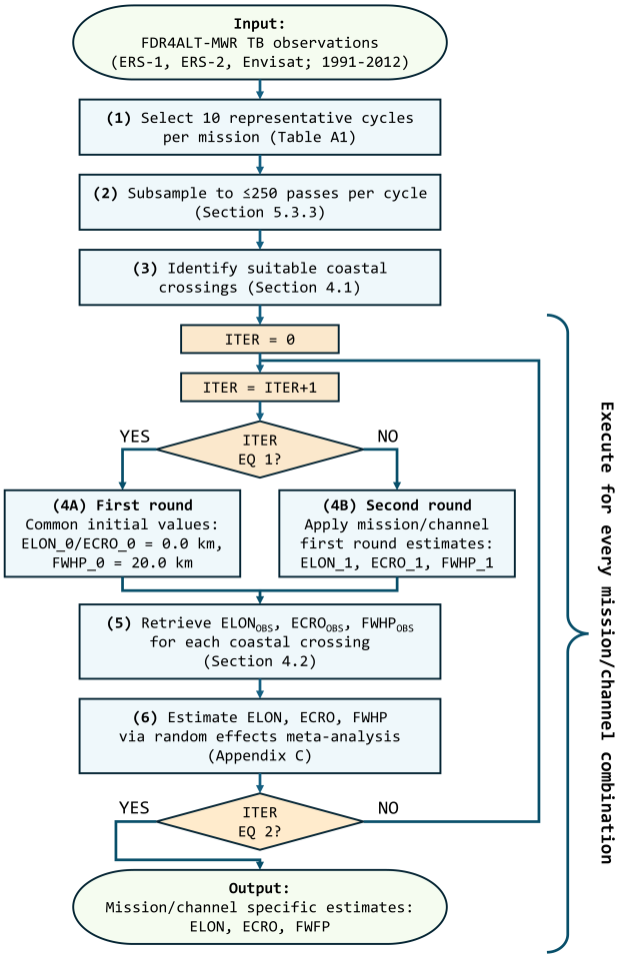

Figure 10. Schematic of the two-round iterative methodology for estimating ELON, ECRO, and FWHP. Notation follows standard flowchart conventions: rounded rectangles denote start/end points; diamonds denote decisions; rectangles denote processing steps. Mathematical details are provided in Appendix C.

In the first round, nominal footprint parameters (ELON = 0.0 km, ECRO = 0.0 km, FWHP = 20.0 km) are applied uniformly across all instruments and channels. Through statistical aggregation, apparent errors arising from parameter interdependence tend to cancel (Sect. 5.2), yielding initial estimates that approximate the true values, albeit with significant uncertainties.

In the second round, these first-round estimates replace the nominal values to refine geolocation and footprint characterisation, thereby reducing residual parameter crosstalk and improving retrieval precision. The resulting estimates and uncertainties for ELON, ECRO, and FWHP constitute the final values reported in this study. Testing additional iterations showed negligible improvement, confirming that two iterative rounds are sufficient to achieve stable values.

https://doi.org/10.5194/egusphere-2026-994
Preprint. Discussion started: 16 March 2026

5.3.3 Input selection and screening

Ten observation cycles per mission are selected to capture environmental variability and potential instrumental changes (Table A1). Nominal cycles span 35 days and comprise 1,002 passes, though four 3-day ERS-1 cycles are also included to extend temporal coverage of the early mission phase. For computational efficiency, the nominal 35-day cycles are randomly subsampled to 250 passes, while shorter 3-day ERS-1 cycles are retained in full.

For each cycle, retrievals are calculated for all coastal crossings meeting the quality requirements defined in Sect. 4.1. Prior to per-cycle aggregation, two further quality filters are applied.

- Outlier rejection: Retrievals beyond ±2.5 σ from the cycle mean are discarded (~1–2 % of data).
- Correlation threshold: Retrievals with TB—ELF correlation $r < 0.999$ are rejected (~5–10 % of data).

The stringent correlation threshold reflects the expectation of very high TB—ELF correlation given the pronounced brightness temperature contrast between land and water surfaces; high-quality crossings, characterised by suitable coastal morphology and the absence of significant environmental noise, typically yield $r > 0.9995$. These filters ensure robust input for statistical analysis while maintaining sufficient sample size, typically yielding 250–300 retrievals per cycle.

5.4 Characterisation of retrieval precision

5.4.1 Empirical variance modelling

The per-cycle aggregation (Sect. 5.3) employs empirical variance models to characterise retrieval uncertainty as a function of the coastal crossing angle. Separate models are developed for all 18 combinations of platform, channel, and parameter.

Retrieval precision is assumed to be invariant for opposing crossing directions and, on average, for crossing angles mirrored about the coastal normal. This symmetry allows the full range [−360°, 360°] to be mapped onto the [0°, 90°] interval.

Figure 11 illustrates the variance model development the ERS-1 23.8 GHz channel, as well as its evolution from first to second iterative round. For a given instrument-channel-parameter combination, the variance model is built via piecewise linear interpolation between the mean variances from the 15° bins. To ensure coverage of the full 0° to 90° range, retrievals for crossing angles <7.5° or >82.5° are assigned the variance of the nearest bin. The second-round variance models provide the uncertainty basis for the per-cycle aggregation (Eq. (C1) in Appendix C1).

5.4.2 Analysis of iterative improvements

The angular dependence of the retrieval precision (inverse of variance) after the second iteration aligns with the theoretical framework described in Sect. 3.4. As shown in Fig. 11, the iterative process yields substantial gains in both data yield and precision across all parameters.

ELON (Fig. 11a,b) is retrieved with the highest precision among all parameters, benefitting from abundant crossings under near-perpendicular angles and correspondingly reduced impact of error interdependence. Consequently, the improvements between first and second rounds are modest: the number of retained (i.e., quality-screened, Sect. 5.3.3) individual $ELON_{OBS}$ retrievals increases by approximately 1.5 % from N = 2,629 to N = 2,669 while the variance is only slightly reduced, mainly for coastal crossing angles above 40°.

In contrast, ECRO (Fig. 11c,d) shows peak precision for crossing angles between 40° and 60°. First-round $ECRO_{OBS}$ retrievals exhibit a significantly higher standard deviation (±5–10 km compared to ±1–2 km for $ELON_{OBS}$), as well as a bimodal distribution with symmetric positive and negative branches. The highest spread occurs at near-perpendicular crossings ($\theta \approx 0°$), as theoretically expected; this split results from apparent across-track errors ($ECRO_{APP}$) induced by the along-track displacement (ELON), with the sign depending on the crossing geometry (Sect. 3.4). By incorporating first-round ELON

https://doi.org/10.5194/egusphere-2026-994
Preprint. Discussion started: 16 March 2026

estimates into the second round, the bimodal distribution collapses into a single mode, the number of retained retrievals increases by approximately 20 % (from N = 2,138 to N = 2,578), and variance is reduced by a factor of 3 to 5.

FWHP (Fig 11e,f) retrieval is highly sensitive to geolocation errors because small misalignments in position can significantly alter the footprint size required to maximise TB—ELF correlation, resulting in the smallest number (N = 708) of retained first-round retrievals. Applying first-round estimates of ELON and ECRO in the second iteration yields substantial improvements: The number of retained retrievals more than triples to N = 2,417 while variance is substantially reduced.

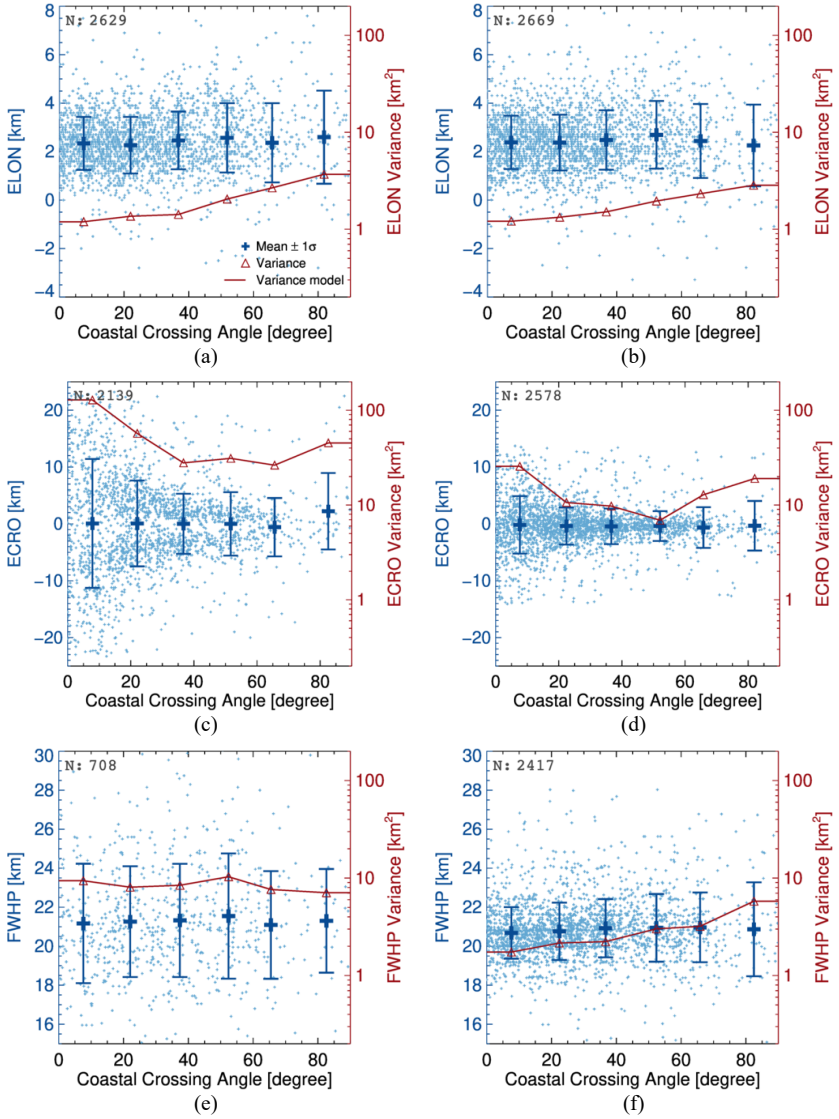

Figure 11. Empirical variance models for the ERS-1 23.8 GHz channel for ELON (a, b), ECRO (c, d), and FWHP (e, f). The left column (a, c, e) shows first-round retrievals using a common nominal footprint; the right column (b, d, f) displays second-round retrievals using individually optimised footprints. Each panel presents means with standard deviations and the corresponding variances for 15° crossing angle bins, with the resulting variance model overlaid. The underlying individual retrievals are represented as blue dots.

While uncertainties are significantly reduced in the second round, the mean values per coastal crossing angle bin do not change substantially for any parameter. This demonstrates the robustness of the statistical approach: while individual retrievals

https://doi.org/10.5194/egusphere-2026-994
Preprint. Discussion started: 16 March 2026

improve with better initial estimates (thereby reducing uncertainty), the ensemble averages converge consistently, exhibiting weak dependence on starting conditions.

6 Results

6.1 Geolocation and footprint estimates

Applying the retrieval procedure described in Sect. 5 yields the mission- and channel-specific estimates for ELON, ECRO, and FWHP presented in Table 2.

Table 2. ELON, ECRO and FWHP estimates (mean ± 1 σ). N indicates the total number of retrievals used per aggregation. The geolocation error represents the length of the vector generated from combining the orthogonal ELON and ECRO contributions.

Satellite	Channel [GHz]	ELON [km]	ECRO [km]	Geolocation error [km]	FWHP [km]
ERS-1	23.8	+2.38±0.07 N=2,669	-0.32±0.08 N=2,578	2.40±0.07	20.80±0.04 N=2,417
ERS-1	36.5	+1.46±0.05 N=2,690	-0.17±0.07 N=2,607	1.47±0.05	21.40±0.04 N=2,579
ERS-2	23.8	+1.60±0.05 N=2,583	+1.12±0.08 N=2,518	1.95±0.06	20.48±0.03 N=2,144
ERS-2	36.5	+1.38±0.10 N=2,716	+1.08±0.12 N=2,643	1.75±0.11	21.78±0.04 N=2,548
Envisat	23.8	+0.30±0.06 N=3,727	-1.00±0.08 N=3,578	1.04±0.08	20.72±0.04 N=3,558
Envisat	36.5	-0.06±0.08 N=3,423	-1.10±0.06 N=3,404	1.10±0.06	18.59±0.04 N=2,975

The results reveal systematic differences between missions and channels.

- ERS-1 exhibits geolocation errors dominated by forward along-track offsets, with significant differences between channels. FWHP estimates differ by ~0.6 km, with the 23.8 GHz channel yielding the smaller footprint.
- ERS-2 shows more uniform geolocation errors across channels, resulting from moderate forward along-track and leftward across-track offsets. FWHP estimates differ by ~1.3 km, again with the smaller size for the 23.8 GHz channel.
- Envisat achieves the highest geolocation accuracy, almost identical in both channels, resulting from near-zero along-track and moderate rightward across-track offsets. FWHP estimates differ by ~2.1 km --more than for the ERS missions-- with the 36.5 GHz channel showing the smaller size, reflecting its modified antenna design (Sect. 2.1).

These findings suggest progressive improvements in positioning accuracy from ERS to Envisat. However, even for Envisat, geolocation correction remains critical for coastal applications demanding sub-kilometre precision.

6.2 Temporal stability

We assess the temporal stability of the footprint characterisation using the nonparametric Mann-Kendall (MK) test (Gilbert, 1987), which evaluates monotonic trends by analysing the sign of differences between all possible data pairs. This approach is particularly suitable for our repeat cycle-based analysis, as it accommodates missing values and irregular temporal spacing without requiring specific distributional assumptions. Following (Nikolakopoulos et al., 2023), we treat differences smaller than the combined measurement uncertainty as statistically tied observations.

The MK test computes Kendall's *S* statistic, which is standardised by its variance to yield a *Z*-score, . approximating a standard normal distribution under the null hypothesis of no trend. This enables the calculation of a two-tailed *p*-value, representing the probability of observing a trend of the measured magnitude assuming no true systematic trend exists.

https://doi.org/10.5194/egusphere-2026-994
Preprint. Discussion started: 16 March 2026

We adopt a significance level of $\alpha = 0.10$ to evaluate the null hypothesis (H_0, no monotonic trend). This elevated threshold (relative to the conventional 0.05) is chosen to compensate for the limited statistical power inherent in our small sample size ($N = 10$). This approach prioritises the detection of subtle sensor drifts or system degradations over the minimisations of Type I errors (false positives). Consequently, a p-value < 0.10 indicates a statistically significant trend.

Figure 12a exemplarily shows the temporal evolution of ELON and ECRO for ERS-1's 23.8 GHz channel. The values summarised in Table 3 confirm the absence of statistically significant trends at $\alpha = 0.10$ for both parameters (ELON: $p = 0.47$; ECRO: $p = 1.00$), with fluctuations falling within the range of observational noise.

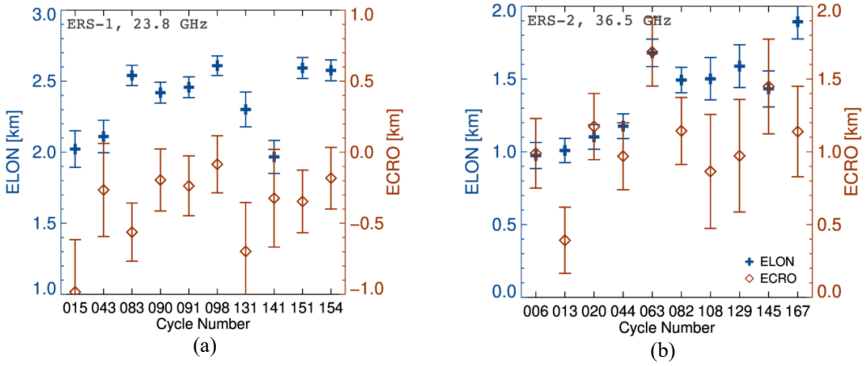

Figure 12. Temporal evolution of ELON and ECRO. (a) ERS-1 at 23.8 GHz, showing no significant trends between September 1991 (cycle 015) and March 1996 (cycle 154). (b) ERS-2 at 36.5 GHz exhibiting a significant trend in ELON (p=0.03), driven by a marked increase between August 1999 (cycle 044) and April 2001 (cycle 063). No corresponding trend is observed for ECRO (p=0.65).

Across all combinations of satellites, channels, and parameters, only ELON for ERS-2 at 36.5 GHz exhibits a significant trend at $\alpha = 0.10$ (Fig. 12b), driven by a pronounced increase between cycles 044 (August 1999) and 063 (April 2001). This degradation coincides with the sequential failure of the ERS-2 gyroscopes between February 2000 and January 2001, which prompted the transition to the "Extra-Backup Mode" for gyro-less attitude control (Miranda et al., 2004).

Table 3. Trend analysis for ELON, ECRO, and FWHP using the Mann-Kendall test. Parameters showing p-values below α = 0.10 exhibit statistically significant temporal trends. Symbols indicate trend direction: significant upward (▲), non-significant upward or downward (△, ▽).

Satellite	Channel [GHz]	ELON [p-value]	ECRO [p-value]	FWHP [p-value]
ERS-1	23.8	0.47 (△)	1.00 (▽)	0.93 (▽)
ERS-1	36.5	0.42 (△)	1.00 (▽)	1.00 (▽)
ERS-2	23.8	0.37 (△)	0.72 (△)	0.79 (▽)
ERS-2	36.5	**0.03 (▲)**	0.65 (△)	1.00 (▽)
Envisat	23.8	0.53 (▽)	0.47 (▽)	0.59 (▽)
Envisat	36.5	0.21 (△)	1.00 (▽)	p1.00 (▽)

To account for this discontinuity, we provide separate ELON estimates in Table 4, distinguishing between periods before (cycles ≤ 044) and after (cycles ≥ 063) the gyroscope failures. Although only the ERS-2 36.5 GHz channel exhibits a statistically significant trend, we include parallel split-period estimates for the ERS-2 23.8 GHz channel to ensure a consistent geolocation correction strategy across both channels.

https://doi.org/10.5194/egusphere-2026-994
Preprint. Discussion started: 16 March 2026

Table 4. ERS-2 ELON estimates (mean ± 1σ) before and after gyroscope failure, accounting for the gyroscope-related attitude-control discontinuity.

Satellite	Channel [GHz]	Applies to cycles	ELON [km]
ERS-2	23.8	≤ 044	1.46 ± 0.13
ERS-2	23.8	≥ 063	1.71 ± 0.13
ERS-2	36.5	≤ 044	1.07 ± 0.15
ERS-2	36.5	≥ 063	1.60 ± 0.14

6.3 Footprint characterisation

Our retrieval assumes circular footprints (Sect. 3.1), reflecting the near-nadir geometry of MWR observations. However, deviations from circularity may arise — for example, from residual errors in sidelobe correction or antenna pattern asymmetries. A more detailed footprint characterisation can be achieved by analysing how the retrieved FWHP varies with coastal crossing angle θ.

When we determine the footprint's 3-dB width across a coastal transition at an angle θ from correlation analysis, we are effectively retrieving the 1D-projected width of the 2D-footprint onto the normal of the coastline. We model the footprint's effective diameter D (i.e., the retrieved FWHP) as a function of crossing angle θ:

$$D(\theta) = 2\sqrt{\left(a\cos\left(\theta-\phi_0\right)\right)^2 + \left(b\sin\left(\theta-\phi_0\right)\right)^2}\,, \tag{5}$$

where a and b are the semi-major and semi-minor axes of the elliptical 3-dB contour and ϕ_0 is the orientation of the ellipse's major axis relative to the satellite's ground track azimuth. We then fit Eq. (5) to the six data points (θ_i, D_i) per instrument and channel derived when establishing the variance models (Sect. 5.4) using the non-linear least squares solver MPFIT (Markwardt, 2009; Moré, 1978). Because the footprints are near-circular, the orientation angle is ill-defined; we therefore fix $\phi_0 = 0$.

The results, summarised in Table 5, reveal inter-mission and inter-channel differences in footprint geometry, with aspect ratios (a/b) ranging from 0.94 to 1.06. *Note that the circular FWHP estimates are consistently closer to the along-track than to the across-track values, reflecting the predominance of individual FWHP retrievals at small crossing angles (Sect. 5.2).*

Table 5. Footprint dimensions and aspect ratios for ERS-1, ERS-2 and Envisat. FWHP values retrieved assuming circular footprints are shown for reference.

Mission	Channel [GHz]	Circular FWHP [km]	Along-track (2×a) FWHP [km]	Across-track (2×b) FWHP [km]	Aspect ratio *a/b*
ERS-1	23.8	20.80 ± 0.04	20.7 ± 0.6	21.0 ± 0.6	0.99
ERS-1	36.5	21.40 ± 0.04	21.6 ± 0.6	21.0 ± 0.7	1.03
ERS-2	23.8	20.48 ± 0.03	20.3 ± 0.4	20.9 ± 0.4	0.97
ERS-2	36.5	21.78 ± 0.04	22.1 ± 0.6	20.9 ± 0.7	1.06
Envisat	23.8	20.72 ± 0.04	20.6 ± 0.6	21.1 ± 0.6	0.98

https://doi.org/10.5194/egusphere-2026-994
Preprint. Discussion started: 16 March 2026

Envisat	36.5	18.59 ± 0.04	18.3 ± 0.7	19.4 ± 0.6	0.94

As illustrated in Fig. 13, these aspect ratios correspond to maximum departures from circularity ranging from ~0.2 km (ERS-1, 23.8 GHz) to ~0.9 km (ERS-2, 36.5 GHz). Qualitatively, the retrieved aspect ratios for ERS-1 and -2 are consistent with the pre-launch characterisation given by (Bernard et al., 1993; see Table 1). For Envisat, where no detailed pre-launch footprint characterisation is available, we find near-circularity for the 23.8 GHz channel but mild along-track flattening for the 36.5 GHz channel (a/b ≈ 0.94).

Residuals between model and observations increase for crossing angles θ larger than ~75°, indicating higher-order asymmetries in the antenna pattern not captured by the elliptical approximation. A more precise in-orbit characterisation using the presented approach would require a dedicated investigation involving a larger number of coastal overpasses and rigorous screening for morphologically simple coastlines, enabling finer angular resolution and reduced uncertainties.

The impact of the observed deviations from footprint circularity is application dependent. For example, in geolocation assessments, where the position is identified by the TB—ELF correlation maximum, we do not expect a significant impact because ellipse symmetry on average preserves the location of the correlation peak. In contrast, when correcting individual observations for land contamination, where exact knowledge of the effective land fraction within the footprint is required, unaccounted ellipticity can introduce systematic errors.

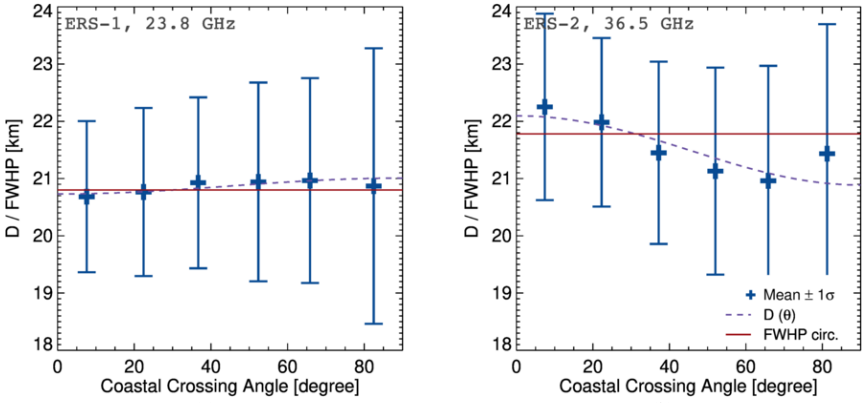

Figure 13. Retrieved effective footprint diameter (D) as a function of coastal crossing angle θ. (a) ERS-1, 23.8 GHz, exhibiting minimum deviation from circularity (a/b ≈ 0.99). (b) ERS-2, 36.5 GHz, exhibiting maximum along-track elongation (a/b ≈ 1.06). Horizontal red lines indicate the mean FWHP retrieved under the circular footprint assumption.

7 Conclusions

This study presents a systematic in-orbit characterisation of the effective footprint geolocation and spatial characteristics of the MWR instruments onboard ERS-1, ERS-2, and Envisat. It is based on the Fundamental Data Record for Radiometry (FDR4RAD_V1) — ESA's current reference dataset for ERS and Envisat MWR observations. By analysing coastal crossings from more than 26,000 half-orbits spanning nearly 30 years, we have developed a methodology to isolate instrument-specific characteristics from environmental noise.

Our analysis reveals systematic geolocation offsets across all missions and channels (Table 2). Along-track deviations range from -0.06 ± 0.08 km (backward) to +2.38 ± 0.07 km (forward), while across-track errors vary from -1.10 ± 0.06 km (rightward) to +1.12 ± 0.08 km (leftward). Combined geolocation errors (ELON and ECRO via RSS) show progressive improvements from 2.40 ± 0.07 km (ERS-1, 23.8 GHz) to 1.04 ± 0.08 km (Envisat, 23.8 GHz). The consistently low standard errors, on the order of 0.1 km, demonstrate the good precision of the coastal crossing method when applied to a sufficiently large dataset. At

https://doi.org/10.5194/egusphere-2026-994
Preprint. Discussion started: 16 March 2026

an orbital altitude of 800 km, this level of ground-track geolocation uncertainty translates to an instrument pointing precision of approximately 0.01 degree.

Statistical analysis confirms the temporal stability of the geolocation offsets at a significance level of $\alpha = 0.10$ for all but one parameter: ERS-2's 36.5 GHz channel exhibits a statistically significant trend in ELON ($p = 0.03$), temporally coincident with gyroscope failures and subsequent transition to the gyro-less "Extra-Backup Mode". To maintain data quality across this transition, we provide ERS-2-specific geolocation corrections for pre- and post-failure periods. The sensitivity of the method to these platform changes indicates its utility as a diagnostic tool for monitoring instrument health and platform stability over a mission's lifetime.

We characterise footprint size through 2D Gaussian circular fits, yielding FWHP estimates ranging from 18.59 ± 0.04 km (Envisat, 36.5 GHz) to 21.78 ± 0.04 km (ERS-2, 36.5 GHz). Subsequent analysis of footprint geometry yields aspect ratios between 0.94 and 1.06, indicating modest but distinct instrument- and channel-dependent deviations from circularity. While the elliptical approximation adequately captures the effective antenna pattern for crossing angles up to ~75°, the observed residuals beyond this range suggest higher-order asymmetries that warrant further dedicated characterisation.

The achieved improvements in geolocation and footprint characterisation enhance the alignment between brightness temperature observations and corresponding effective land fractions, enabling more precise correction for land contamination. Application of the geolocation correction is straightforward: subtract the values for ELON and ECRO from the nominal geolocations in the FDR4RAD_V1 product.

The presented methodology provides a standardised framework for the in-orbit characterisation of near-nadir-looking passive microwave radiometers supporting altimetry. It is directly transferable to contemporary missions such as Sentinel-3 and Sentinel-6, thereby supporting the cross-mission consistency required for building multi-decadal sea-level records. By refining our understanding of footprint geolocation and geometry, this approach can contribute to more reliable wet tropospheric corrections in coastal zones, helping to maintain data continuity across legacy and modern altimetry missions.

Appendix A

Table A1: Repeat cycles analysed for each MWR mission.

Platform	Cycle	No. of passes	Start	End
ERS-1	015	81	1991-09-09	1991-09-12
ERS-1	043	86	1991-12-02	1991-12-05
ERS-1	083	817	1992-03-31	1992-05-01
ERS-1	090	959	1992-11-27	1992-12-31
ERS-1	091	996	1993-01-01	1993-02-05
ERS-1	098	977	1993-09-03	1993-10-08
ERS-1	131	86	1994-03-18	1994-03-21
ERS-1	141	108	1994-09-28	1994-10-01
ERS-1	151	989	1995-11-05	1995-12-10
ERS-1	154	999	1996-02-18	1996-03-24
ERS-2	006	998	1995-11-06	1995-12-11
ERS-2	013	990	1996-07-08	1996-08-12
ERS-2	020	998	1997-03-10	1997-04-14
ERS-2	044	998	1999-06-28	1999-08-02
ERS-2	063	921	2001-04-23	2001-05-28
ERS-2	082	995	2003-02-17	2003-03-24
ERS-2	108	842	2005-08-15	2005-09-19
ERS-2	129	969	2007-08-20	2007-09-24

https://doi.org/10.5194/egusphere-2026-994
Preprint. Discussion started: 16 March 2026

Platform	Cycle	No. of passes	Start	End
ERS-2	145	901	2009-03-02	2009-04-06
ERS-2	167	781	2011-04-11	2011-05-16
Envisat	007	895	2002-06-17	2002-07-22
Envisat	014	801	2003-02-17	2003-03-24
Envisat	029	991	2004-07-26	2004-08-30
Envisat	038	999	2005-06-06	2005-07-11
Envisat	048	979	2006-05-22	2006-06-26
Envisat	060	916	2007-07-16	2007-08-20
Envisat	067	935	2008-03-17	2008-04-21
Envisat	083	988	2009-09-28	2009-11-02
Envisat	090	999	2010-05-31	2010-07-05
Envisat	107	861	2011-09-22	2011-10-22

Appendix B: Effective land fraction

B1 Antenna pattern approximation

The antenna pattern (AP) is approximated as a 2D Gaussian:

$$\mathrm{AP}(x,y)=\begin{cases}\frac{1}{2\pi\sigma^2}\times\exp\left(-\frac{x^2+y^2}{2\sigma^2}\right), & if\ \sqrt{x^2+y^2}\le c\times\frac{\mathrm{FWHP}}{2}\\ 0, & if\ \sqrt{x^2+y^2}>c\times\frac{\mathrm{FWHP}}{2}\end{cases}, \tag{B1}$$

where x and y are surface coordinates relative to the beam centre, c defines the AP truncation as a multiple of FWHP, and σ is the Gaussian standard deviation. The relationship between σ and FWHP is given by:

$$\mathrm{FWHP}=2\sigma\sqrt{2\ln 2}\approx 2.355\times\sigma \tag{B2}$$

The total power P enclosed within a radius r from the beam centre is:

$$P(r)=1-\exp\left(-\frac{r^2}{2\sigma^2}\right) \tag{B3}$$

For this study, we truncate AP at $c = 2.5$, corresponding to $r = 1.25 \times$ FWHP. Substituting FWHP through Eq. (B2) yields $r \approx 2.944 \times \sigma$ and, via Eq. (B3), an enclosed power fraction of $P = 98.7\ \%$.

B2 Convolution with the land-sea mask

The effective land fraction (ELF) at position (i, j) is calculated by convolving the antenna pattern in geographical coordinates $\mathrm{AP}_{\mathrm{GEO}}$ with a binary land-sea mask (LSM; 1 = land, 0 = sea), where the kernel sizes M and N depend on the beam diameter and spatial resolution:

https://doi.org/10.5194/egusphere-2026-994
Preprint. Discussion started: 16 March 2026

$$\mathrm{ELF}(i,j) = \frac{\sum_{m=-M}^{M}\sum_{n=-N}^{N} \mathrm{LSM}[i+m, j+n] \times \mathrm{AP}_{\mathrm{GEO}}[m,n]}{\sum_{m=-M}^{M}\sum_{n=-N}^{N} \mathrm{AP}_{\mathrm{GEO}}[m,n]} \tag{B4}$$

Appendix C: Statistical aggregation

C1 Within-cycle statistics

The arithmetic mean μ_i is chosen as the estimator for the expected value of the i-th cycle:

$$\mu_i = \frac{1}{n_i}\sum_{j=1}^{n_i} y_{ij}\,, \tag{C1}$$

where y_{ij} is the retrieved value (i.e., $\mathrm{ELON_{OBS}}$, $\mathrm{ECRO_{OBS}}$, or $\mathrm{FWHP_{OBS}}$) for the j-th observation in cycle i, and n_i is the total number of observations.

Each observation y_{ij} is assigned an individual variance v_{ij} from an empirical error model $v_{ij} = f(\theta_{ij})$, where θ_{ij} is the coastal crossing angle. The construction and calibration of this variance model, which reflects the angle-dependent precision of the retrieval, are described in Sect. 5.4. The adjusted (propagated) variance of the mean σ_i^2, reflecting both the variability of individual observations and the statistical benefit of averaging, is computed as:

$$\sigma_i^2 = \frac{\sum_{j=1}^{n_i} v_{ij}}{n_i^2}\,. \tag{C2}$$

C2 Fixed effects model

The fixed effects (FE) model is used to combine the cycle means μ_i under the assumption that their within-cycle variances σ_i^2 capture all significant variability. Under this assumption, the optimal method for combining the estimates is inverse-variance weighting (Borenstein et al., 2021), which yields the minimum-variance combined estimate according to the Gauss-Markov theorem.

The weight w_i assigned to each cycle is the inverse of its variance:

$$w_i = \frac{1}{\sigma_i^2}\,, \tag{C3}$$

The overall weighted average μ_{FE} and its variance σ_{FE}^2 are then calculated as:

$$\mu_{FE} = \frac{\sum_{i=1}^{N} w_i\,\mu_i}{\sum_{i=1}^{N} w_i}\,, \tag{C4}$$

https://doi.org/10.5194/egusphere-2026-994
Preprint. Discussion started: 16 March 2026

$$\sigma_{FE}^2 = \frac{1}{\sum_{i=1}^{N} w_i}, \tag{C5}$$

where N is the total number of observation cycles. This weighting scheme automatically assigns greater weight to cycles with more precise means (smaller σ_i^2), which typically correspond to cycles with larger sample sizes or a greater proportion of favourable retrieval conditions.

C3 Random-effects meta-analysis

When significant sources of variability exist between cycles beyond those accounted for in the per-cycle variances σ_i^2, the fixed effects model underestimates the total uncertainty. The random-effects (RE) model addresses this by introducing a between-cycle variance term τ^2, which captures this additional heterogeneity (Borenstein et al., 2021).

The between-cycle variance τ^2 is estimated using the DerSimonian-Laird estimator (DerSimonian and Laird, 2015), quantifying the excess variability by comparing the observed heterogeneity among cycle means to the heterogeneity expected under the fixed effects assumption. First, the heterogeneity statistic (Cochran's Q) is first calculated as:

$$Q = \sum_{i=1}^{N} w_i \left(\mu_i - \mu_{FE}\right)^2 \tag{C6}$$

where μ_{FE} is the fixed effects mean from Eq. (C4). The DerSimonian-Laird estimator for τ^2 is then:

$$\tau^2 = \max\left(0, \frac{Q-(N-1)}{\sum_{i=1}^{N} w_i - \frac{\sum_{i=1}^{N} w_i^2}{\sum_{i=1}^{N} w_i}}\right). \tag{C7}$$

When $Q \le (N\text{-}1)$, the observed heterogeneity is consistent with sampling variability under the fixed effects assumption, and τ^2 is set to zero, causing the RE model to reduce to the FE model.

Adjusted weights incorporate both within-cycle and between-cycle variances:

$$w_i^{RE} = \frac{1}{\sigma_i^2 + \tau^2}. \tag{C8}$$

These weights are used to calculate the random-effects weighted average μ_{RE} and its variance σ_{RE}^2 analogously to the fixed-effects case, using Eqs. (C4) and (C5) with w_i^{RE} in place of w_i^{FE}.

Data availability

This study uses the following publicly available datasets:

https://doi.org/10.5194/egusphere-2026-994
Preprint. Discussion started: 16 March 2026

- Fundamental Data Record for Radiometry, Version 1 (FDR4RAD_V1): https://doi.org/10.5270/esa-79a176b (FDR4ALT-MWR, 2024)
- Global Land Mask for Satellite Ocean Colour Remote Sensing: https://doi.org/10.17632/9r93m9s7cw.1 (Mikelsons et al., 2021)
- Global database of Coastal Characteristics (GCC): https://doi.org/10.5281/zenodo.11072020 (Athanasiou et al., 2024)

The geolocation corrections and footprint characterisation results derived in this study are provided in Tables 2–5.

Supplement link

Does not apply.

Team list

Does not apply.

Author contributions

All authors jointly conceived the study. FF developed the methodology, implemented the software, performed the formal analysis, created the visualisations, and prepared the initial version of the manuscript. All authors then contributed to the review and the editing of the final manuscript.

Competing interests

The authors declare that they have no conflict of interest.

Disclaimer

Copernicus Publications remains neutral with regard to jurisdictional claims made in the text, published maps, institutional affiliations, or any other geographical representation in this paper. While Copernicus Publications makes every effort to include appropriate place names, the final responsibility lies with the authors. Views expressed in the text are those of the authors and do not necessarily reflect the views of the publisher.

Acknowledgements

This work was supported by ESA through the FDR4ALT project, which also funded the generation of the FDR4RAD_V1 dataset by CLS. Initial ideas were developed earlier in the context of the AMTROC activities funded by EUMETSAT. Generative AI was used for assisting with text editing and the implementation of statistical tools.

Financial support

Does not apply.

Review statement

To be added by Copernicus.

https://doi.org/10.5194/egusphere-2026-994
Preprint. Discussion started: 16 March 2026

References

Aguiar, P., Vieira, T., Lázaro, C., and Fernandes, M. J.: An Improved Altimetry Wet Tropospheric Correction Retrieval Over Coastal Regions for the Sentinel-3 Mission, IEEE J. Sel. Top. Appl. Earth Observations Remote Sensing, 16, 7979–7991, https://doi.org/10.1109/JSTARS.2023.3308721, 2023.

Athanasiou, P., Van Dongeren, A., Pronk, M., Giardino, A., Vousdoukas, M., and Ranasinghe, R.: Global Coastal Characteristics (GCC): a global dataset of geophysical, hydrodynamic, and socioeconomic coastal indicators, Earth Syst. Sci. Data, 16, 3433–3452, https://doi.org/10.5194/essd-16-3433-2024, 2024.

Atkinson, N. C., Bombaci, O., L'Abbate, M., and Ricketts, M.: ENVISAT-1 MWR: calibration targets and preflight calibration, in: SPIE Proceedings, Remote Sensing, Barcelona, Spain, 141–152, https://doi.org/10.1117/12.333625, 1998.

Bennartz, R.: On the Use of SSM/I Measurements in Coastal Regions, J. Atmos. Oceanic Technol., 16, 417–431, https://doi.org/10.1175/1520-0426(1999)016%253C0417:OTUOSI%253E2.0.CO;2, 1999.

Bernard, R., Le Cornec, A., Eymard, L., and Tabary, L.: The microwave radiometer aboard ERS-1.1. Characteristics and performances, IEEE Trans. Geosci. Remote Sensing, 31, 1186–1198, https://doi.org/10.1109/36.317444, 1993.

Bevis, M., Businger, S., Herring, T. A., Rocken, C., Anthes, R. A., and Ware, R. H.: GPS meteorology: Remote sensing of atmospheric water vapor using the global positioning system, J. Geophys. Res., 97, 15787–15801, https://doi.org/10.1029/92jd01517, 1992.

Borenstein, M., Hedges, L. V., Higgins, J., and Rothstein, H. R.: Introduction to meta-analysis, Second edition., Wiley, Hoboken, NJ Chichester, 500 pp., 2021.

Brockley, D. J., Baker, S., Femenias, P., Martinez, B., Massmann, F.-H., Otten, M., Paul, F., Picard, B., Prandi, P., Roca, M., Rudenko, S., Scharroo, R., and Visser, P.: REAPER: Reprocessing 12 Years of ERS-1 and ERS-2 Altimeters and Microwave Radiometer Data, IEEE Trans. Geosci. Remote Sensing, 55, 5506–5514, https://doi.org/10.1109/tgrs.2017.2709343, 2017.

Brown, S.: A Novel Near-Land Radiometer Wet Path-Delay Retrieval Algorithm: Application to the Jason-2/OSTM Advanced Microwave Radiometer, IEEE Trans. Geosci. Remote Sensing, 48, 1986–1992, https://doi.org/10.1109/TGRS.2009.2037220, 2010.

Chelton, D. B., Ries, J. C., Haines, B. J., Fu, L.-L., and Callahan, P. S.: Chapter 1 Satellite Altimetry, in: International Geophysics, Elsevier, 1–ii, https://doi.org/10.1016/s0074-6142(01)80146-7, 2001.

DerSimonian, R. and Laird, N.: Meta-analysis in clinical trials revisited, Contemporary Clinical Trials, 45, 139–145, https://doi.org/10.1016/j.cct.2015.09.002, 2015.

Desportes, C., Obligis, E., and Eymard, L.: One-Dimensional Variational Retrieval of the Wet Tropospheric Correction for Altimetry in Coastal Regions, IEEE Trans. Geosci. Remote Sensing, 48, 1001–1008, https://doi.org/10.1109/TGRS.2009.2031494, 2010.

Desportes, C. ., Obligis, E. ., and Eymard, L. .: On the Wet Tropospheric Correction for Altimetry in Coastal Regions, IEEE Trans. Geosci. Remote Sensing, 45, 2139–2149, https://doi.org/10.1109/TGRS.2006.888967, 2007.

Drinkwater, M. R. and Rebhan, H.: Sentinel-3: Mission Requirements Document, ESA, 2007.

ESA: ENVISAT RA2/MWR Product Handbook, European Space Agency, 2007.

Eymard, L., Obligis, E., Ngan Tran, Karbou, F., and Dedieu, M.: Long-term stability of ERS-2 and TOPEX microwave radiometer in-flight calibration, IEEE Trans. Geosci. Remote Sensing, 43, 1144–1158, https://doi.org/10.1109/TGRS.2005.846129, 2005.

FDR4ALT-MWR: FDR for Radiometry, https://doi.org/10.5270/esa-79a176b, 2024.

Fernandes, M. J., Lázaro, C., Ablain, M., and Pires, N.: Improved wet path delays for all ESA and reference altimetric missions, Remote Sensing of Environment, 169, 50–74, https://doi.org/10.1016/j.rse.2015.07.023, 2015.

Gilbert, R. O.: Statistical methods for environmental pollution monitoring, Wiley, New York Chichester Weinheim, 320 pp., 1987.

https://doi.org/10.5194/egusphere-2026-994
Preprint. Discussion started: 16 March 2026

Karbou, F., Aires, F., Prigent, C., and Eymard, L.: Potential of Advanced Microwave Sounding Unit-A (AMSU-A) and AMSU-B measurements for atmospheric temperature and humidity profiling over land, J. Geophys. Res., 110, 2004JD005318, https://doi.org/10.1029/2004JD005318, 2005.

Markwardt, C. B.: Non-linear Least Squares Fitting in IDL with MPFIT, https://doi.org/10.48550/ARXIV.0902.2850, 2009.

Mikelsons, K., Wang, M., Wang, X.-L., and Jiang, L.: Global land mask for satellite ocean color remote sensing, Remote Sensing of Environment, 257, 112356, https://doi.org/10.1016/j.rse.2021.112356, 2021.

Miranda, N., Rosich, B., Santella, C., and Grion, M.: Review of the Impact of ERS-2 Piloting Modes on the SAR Doppler Stability, in: Proceedings of the FRINGE 2003 Workshop, FRINGE 2003 Workshop, 1-5 December 2003, ESA/ESRIN, Frascati, Italy, 2004.

Moré, J. J.: The Levenberg-Marquardt algorithm: Implementation and theory, in: Numerical Analysis, vol. 630, edited by: Watson, G. A., Springer Berlin Heidelberg, Berlin, Heidelberg, 105–116, https://doi.org/10.1007/BFb0067700, 1978.

Nikolakopoulos, S., Cator, E., and Janssen, M. P.: Extending the Mann–Kendall test to allow for measurement uncertainty, Statistics, 57, 577–596, https://doi.org/10.1080/02331888.2023.2214942, 2023.

Obligis, E., Eymard, L., Tran, N., Labroue, S., and Femenias, P.: First Three Years of the Microwave Radiometer aboard Envisat: In-Flight Calibration, Processing, and Validation of the Geophysical Products, Journal of Atmospheric and Oceanic Technology, 23, 802–814, https://doi.org/10.1175/JTECH1878.1, 2006.

Piras, F., Fréry, M.-L., and Roinard, H.: FDR4ALT Product User Guide, ESA, 2023.

Rouault, E., Warmerdam, F., Schwehr, K., Kiselev, A., Butler, H., Łoskot, M., Szekeres, T., Tourigny, E., Landa, M., Miara, I., Elliston, B., Chaitanya, K., Plesea, L., Morissette, D., Jolma, A., Dawson, N., Baston, D., de Stigter, C., and Miura, H.: GDAL, , https://doi.org/10.5281/ZENODO.5884351, 2025.

Srinivasan, M. and Tsontos, V.: Satellite Altimetry for Ocean and Coastal Applications: A Review, Remote Sensing, 15, 3939, https://doi.org/10.3390/rs15163939, 2023.

Stum, J., Sicard, P., Carrere, L., and Lambin, J.: Using Objective Analysis of Scanning Radiometer Measurements to Compute the Water Vapor Path Delay for Altimetry, IEEE Trans. Geosci. Remote Sensing, 49, 3211–3224, https://doi.org/10.1109/TGRS.2011.2104967, 2011.